
The Sunyaev-Zel'dovich Effect at Five Arc-seconds: RX J1347.5–1145 Imaged by ALMA

Tetsu KITAYAMA¹, Shutaro UEDA², Shigehisa TAKAKUWA^{3,4}, Takahiro TSUTSUMI⁵, Eiichiro KOMATSU^{6,7}, Takuya AKAHORI³, Daisuke IONO^{8,9}, Takuma IZUMI^{8,9}, Ryohei KAWABE^{8,9,10}, Kotaro KOHNO^{11,12}, Hiroshi MATSUO^{8,9}, Naomi OTA¹³, Yasushi SUTO^{12,14}, Motozaku TAKIZAWA¹⁵, and Kohji YOSHIKAWA¹⁶

¹Department of Physics, Toho University, 2-2-1 Miyama, Funabashi, Chiba 274-8510, Japan; kitayama@ph.sci.toho-u.ac.jp

²Institute of Space and Astronautical Science (ISAS), Japan Aerospace Exploration Agency (JAXA), 3-1-1 Yoshinodai, Chuo, Sagami-hara, Kanagawa 252-5210, Japan

³Department of Physics and Astronomy, Graduate School of Science and Engineering, Kagoshima University, 1-21-35 Korimoto, Kagoshima, Kagoshima 890-0065, Japan

⁴Academia Sinica Institute of Astronomy and Astrophysics, P.O. Box 23-141, Taipei 10617, Taiwan

⁵National Radio Astronomy Observatory, P.O. Box O, Socorro, NM, 87801, USA

⁶Max-Planck-Institut für Astrophysik, Karl-Schwarzschild Str. 1, D-85741 Garching, Germany

⁷Kavli Institute for the Physics and Mathematics of the Universe (Kavli IPMU), The University of Tokyo, 5-1-5 Kashiwanoha, Kashiwa, Chiba 277-8583, Japan

⁸National Astronomical Observatory of Japan, 2-21-1 Osawa, Mitaka, Tokyo 181-8588, Japan

⁹The Graduate University for Advanced Studies (SOKENDAI), 2-21-1 Osawa, Mitaka, Tokyo 181-8588, Japan

¹⁰Department of Astronomy, The University of Tokyo, 7-3-1 Hongo, Bunkyo, Tokyo 113-0033, Japan

¹¹Institute of Astronomy, The University of Tokyo, 2-21-1 Osawa, Mitaka, Tokyo 181-0015, Japan

¹²Research Center for the Early Universe, School of Science, The University of Tokyo, 7-3-1 Hongo, Bunkyo, Tokyo 113-0033, Japan

¹³Department of Physics, Nara Women's University, Kita-uoyanishi-machi, Nara, Nara 630-8506, Japan

¹⁴Department of Physics, The University of Tokyo, 7-3-1 Hongo, Bunkyo, Tokyo 113-0033, Japan

¹⁵Department of Physics, Yamagata University, 1-4-12 Kojirakawa-machi, Yamagata, Yamagata 990-8560, Japan

¹⁶Center for Computational Sciences, University of Tsukuba, 1-1-1 Tennodai, Tsukuba, Ibaraki 305-8577, Japan

Received ; Accepted

Abstract

We present the first image of the thermal Sunyaev-Zel'dovich effect (SZE) obtained by the

Atacama Large Millimeter/submillimeter Array (ALMA). Combining 7-m and 12-m arrays in Band 3, we create an SZE map toward a galaxy cluster RX J1347.5–1145 with 5 arc-second resolution (corresponding to the physical size of $20h^{-1}\text{kpc}$), the highest angular and physical spatial resolutions achieved to date for imaging the SZE, while retaining extended signals out to 40 arc-seconds. The 1σ statistical sensitivity of the image is 0.017 mJy/beam or 0.12 mK_{CMB} at the 5 arc-second full width at half maximum. The SZE image shows a good agreement with an electron pressure map reconstructed independently from the X-ray data and offers a new probe of the small-scale structure of the intracluster medium. Our results demonstrate that ALMA is a powerful instrument for imaging the SZE in compact galaxy clusters with unprecedented angular resolution and sensitivity. As the first report on the detection of the SZE by ALMA, we present detailed analysis procedures including corrections for the missing flux, to provide guiding methods for analyzing and interpreting future SZE images by ALMA.

Key words: cosmology: observations – galaxies: clusters: intracluster medium – radio continuum: general – X-rays: galaxies: clusters – techniques: interferometric

1 Introduction

The Sunyaev-Zel'dovich effect (SZE, Sunyaev & Zel'dovich 1972), inverse Compton scattering of the cosmic microwave background (CMB) photons off hot electrons, offers a powerful probe of cosmic plasma up to high redshifts (see Rephaeli 1995; Birkinshaw 1999; Carlstrom, Holder & Reese 2002; Kitayama 2014 for reviews). The surface brightness of the SZE is independent of the source redshift z for given electron density n_e and temperature T_e and is proportional to $n_e T_e$, whereas that of X-rays varies as $n_e^2(1+z)^{-4}$ with only weak dependence on T_e . The SZE can hence be a unique tool for studying the physics of the intracluster medium, e.g., by detecting shocks (pressure gaps) and very hot gas associated with subcluster mergers (Komatsu et al. 2001; Kitayama et al. 2004; Korngut et al. 2011). The advent of large-area surveys by the South Pole Telescope (SPT) (e.g., Staniszewski et al. 2009; Vanderlinde et al. 2010; Williamson et al. 2011; Reichardt et al. 2013), the Atacama Cosmology Telescope (ACT) (e.g., Hincks et al. 2010; Marriage et al. 2011; Hasselfield et al. 2013), and the Planck satellite (e.g., Planck Collaboration 2011; Planck Collaboration 2013) has enhanced the sample of galaxy clusters observed via the SZE by more than an order of magnitude over the past decade. The caveats of existing observations are limited angular resolution ($> 1'$ in the above mentioned surveys) and sensitivity. Single-dish measurements by the MUSTANG bolometer array have achieved currently the highest angular resolution of $9''$ full width at half maximum (FWHM) for the SZE maps (e.g., Mason et al. 2010; Korngut et al. 2011; Romero et al. 2015; Young et al. 2015), while they are still challenged by point source and atmospheric contamination. Interferometers offer a complementary tool with good control of systematic noise and capability of separating compact sources from the SZE, albeit reduced sensitivity for the sources more extended than the baseline coverage (e.g., Jones et al. 1993; Carlstrom, Joy & Grego 1996; AMI Collaboration 2006; Muchovej et al. 2007; Wu et al. 2009). A recent SZE map obtained by CARMA has a synthesized beam with $10.6'' \times 16.9''$ (Plagge et al. 2013).

With a combination of 7-m and 12-m arrays in Band 3, the Atacama Large Millimeter/submillimeter Array (ALMA) serves as the first instrument to resolve the SZE with an angular resolution of $5''$, as predicted by detailed imaging simulations (Yamada et al. 2012) using hydrodynamic simulation data (Takizawa 2005; Akahori & Yoshikawa 2012). Among currently available frequency bands of ALMA, Band 3 is the most suitable for the SZE imaging owing to the largest field-of-view, the lowest system temperature, and minimal contamination by synchrotron and dust emission. Given that the Total Power Array is still unavailable for continuum observations by ALMA, viable targets are limited to compact distant galaxy clusters.

In this paper, we present the first measurement of the SZE by ALMA. The target is a galaxy cluster RX J1347.5–1145 at $z = 0.451$. Owing to its brightness and compactness, RX J1347.5–1145 is a prime target for imaging observations by the current configuration of ALMA. A number of SZE measurements have been made for this cluster in the past (Komatsu et al. 1999; Pointecouteau et al. 1999; Komatsu et al. 2001; Pointecouteau et al. 2001; Reese et al. 2002; Carlstrom, Holder & Reese 2002; Kitayama et al. 2004; Benson et al. 2004; Zemcov et al. 2007; Mason et al. 2010; Korngut et al. 2011; Zemcov et al. 2012; Plagge et al. 2013; Adam et al. 2014; Sayers et al. 2016). In particular, the Nobeyama Bolometer Array (NOBA; Komatsu et al. 2001) detected a prominent substructure that was not expected from regular morphology of this cluster in the soft-band X-ray image by ROSAT (Schindler et

Table 1. Execution Blocks of Band 3 observations for RX J1347.5–1145. The J1337–1257 flux density at 92GHz was obtained by a power-law fit to the flux at 85, 87, 97, 99 GHz in the ALMA QA2 report, based on the original flux scale using the flux calibrator shown in the table. In EB7-9 and EB12-2, the flux scales using Ceres were not used in the subsequent analysis and replaced by those of EB7-8 and EB12-3, respectively.

ID	Array	Date	Number of Antennas	On-source time [min]	Flux Calibrator	J1337–1257 flux density at 92GHz [Jy]
EB7-1	7-m	2014-08-16	10	39.43	Mars	4.430 ± 0.003
EB7-2	7-m	2014-08-17	10	39.43	Mars	4.745 ± 0.003
EB7-3	7-m	2014-08-17	10	19.97	Mars	4.582 ± 0.002
EB7-4	7-m	2014-08-17	9	39.43	Mars	4.290 ± 0.003
EB7-5	7-m	2014-12-06	7	39.43	J1337–1257	5.041 ± 0.003
EB7-6	7-m	2014-12-11	9	39.43	Callisto	4.416 ± 0.031
EB7-7	7-m	2014-12-15	8	39.43	J1337–1257	4.808 ± 0.001
EB7-8	7-m	2014-12-28	8	39.43	Callisto	5.102 ± 0.067
EB7-9	7-m	2014-12-28	8	39.43	(Ceres)	(3.940 ± 0.016)
EB12-1	12-m	2014-12-15	41	34.13	Ganymede	4.358 ± 0.002
EB12-2	12-m	2014-12-29	39	40.42	(Ceres)	(5.621 ± 0.002)
EB12-3	12-m	2014-12-30	39	40.42	J1337–1257	4.649 ± 0.001
EB12-4	12-m	2015-01-04	40	40.42	J1337–1257	4.916 ± 0.001

al. 1997). The presence of the substructure was confirmed with subsequent X-ray data by Chandra (Allen et al. 2002; Johnson et al. 2012) and XMM-Newton (Gitti and Schindler 2007) as well as SZE maps by MUSTANG (Mason et al. 2010; Korngut et al. 2011), CARMA (Plagge et al. 2013), and NIKA (Adam et al. 2014). The inferred temperature of the substructure exceeds 20 keV and is appreciably higher than the mean temperature of the cluster ~ 13 keV (Kitayama et al. 2004; Ota et al. 2008); this accounts for the fact that the substructure was more obvious in the SZE map than the X-ray surface brightness image. The disturbed feature was also observed by the radio synchrotron observations (Gitti et al. 2007; Ferrari et al. 2011) and gravitational lensing maps (e.g., Miranda et al. 2008; Bradač et al. 2008; Köhlinger and Schmidt 2014). These previous results indicate that the cluster is undergoing a merger, but its exact nature such as geometry and dynamics of the collision is still unclear (Johnson et al. 2012; Kreisch et al. 2016). The ALMA Band 3 observation of RX J1347.5–1145 is crucial not only for better understanding this particular galaxy cluster but also for testing the capability of ALMA in observing the SZE against a range of independent datasets available for this well-studied system.

This paper is organized as follows. Section 2 describes the observations and calibration. Section 3 presents details of the imaging analysis including point source subtraction and deconvolution. The results are validated against the X-ray data, realistic imaging simulations, and previous high-significance SZE measurements in Section 4. Finally, our conclusions are summarized in Section 5. Throughout the paper, we adopt a standard set of cosmological density parameters, $\Omega_M = 0.3$ and $\Omega_\Lambda = 0.7$. We use the dimensionless Hubble constant $h \equiv H_0/(100\text{km/s/Mpc})$; given controversial results on the value of h (e.g., Planck Collaboration 2015; Riess et al. 2016), we do not fix it unless stated otherwise. In this cosmology, the angular size of $1''$ corresponds to the physical size of $4.04 h^{-1}\text{kpc}$ at the source redshift $z = 0.451$. The errors are given in 1σ and the coordinates are given in J2000.

2 Observations and Calibration

RX J1347.5–1145 was observed by ALMA in Band 3 (Project code: 2013.1.00246.S). The data were taken with the 12-m array and the 7-m array at 13 separate Execution Blocks listed in Table 1 between August 2014 and January 2015. Compact configurations were adopted to cover the projected baseline ranges of 7.4–49 m and 12.5–347 m for the 7-m array and the 12-m array, respectively. In all the Execution Blocks, the dual-polarization Time Division Mode was adopted with the central observing frequency of 92 GHz and an effective band width of 7.5GHz; the data were taken at four spectral windows with widths ~ 2 GHz centered at 85, 87, 97, and 99 GHz, respectively. The effective primary beam FWHMs at 92 GHz are $62''$ and $107''$ for 12-m array and 7-m array, respectively. At these frequencies, the above mentioned baseline ranges correspond to the uv distances of 2.1 – 16.3 k λ and 3.5 – 116 k λ for the 7-m array and the 12-m array, respectively. The parameters of the observed maps are summarized in Table 2.

The observing field has a diameter of $\sim 90''$ centered at ($13^{\text{h}}47^{\text{m}}30^{\text{s}}.54, -11^{\text{d}}45^{\text{m}}19.40$), which is about $10''$ south of the X-ray center of RX J1347.5–1145 and is closer to the peak of the offset SZE signal (Komatsu et al. 2001). The field is covered with 7

Table 2. Parameters of observed maps.

Parameters	12-m array	7-m array
Central frequency	92 GHz	92 GHz
Band widths	7.5 GHz	7.5 GHz
Primary beam FWHM at the central frequency	62''	107''
Number of pointings	7	7
Baseline coverage	3.5 – 116 k λ	2.1 – 16.3 k λ
Weighting	natural	natural
Synthesized beam FWHMs	4.1'' \times 2.4''	20.5'' \times 11.1''
Synthesized beam position angle	84.1°	88.1°
Average 1σ noise	0.012 mJy/beam	0.083 mJy/beam

hexagonal mosaic pointings with an equal spacing of 34.2'' by both arrays. This is approximately the Nyquist spacing for the 12-m array and achieves much denser sampling for the 7-m array.

Calibration of the raw visibility data taken with the 12-m array was performed using the Common Astronomy Software Applications (CASA; McMullin et al. 2007) program version 4.3.1 as implemented in a standard reduction script for ALMA Cycle 2 data. The data taken with the 7-m array were calibrated by the ALMA pipeline using the CASA version 4.2.2. We use the data produced from the second stage of ALMA's Quality Assurance process (QA2) for both the 12-m array and the 7-m array.

A quasar J1337–1257 was monitored in all the execution blocks; it is used as a phase calibrator as well as a bandpass calibrator throughout this project. Several solar system objects (Mars, Callisto, Ceres, and Ganymede; see Table 1) were chosen by the observatory as primary flux calibrators, although the data of Ceres were not used in the end for the reason described below. We used these calibrators to determine the flux density of J1337–1257, which was then used to compare the flux scales of different execution blocks.

The Butler-JPL-Horizons-2012 Model (Butler 2012) was used for determining the absolute flux density of solar system objects. The absolute flux densities of J1337–1257 in EB7-5, EB7-7, EB12-3, and EB12-4 were determined from measurements of the solar system objects by the observatory on 2014-12-07, 2014-12-18, and 2015-01-17, available in the ALMA Calibrator Source Catalogue¹. Given that the catalogued measurements were more than 10 days away from EB12-3 and EB12-4, we additionally checked that the flux scales of EB12-3 and EB12-4 were consistent with three calibration measurements of J1337–1257 in Band 3 executed on 2015-01-06, the closest in time available in the ALMA archive, using Ganymede, Pallas, and J1427–421 as flux calibrators (Project codes: 2013.1.00120.S and 2013.1.01312.S).

Flux equalization was applied during QA2 to some of the execution blocks close in time. Observations in August, 2014 (EB7-1, EB7-2, EB7-3, and EB7-4) were performed within 27 hours and scaled together using the mean of the absolute flux scales from the four execution blocks. For EB7-8 and EB7-9 executed within 6 hours, the absolute flux scale of the former was adopted, because the flux calibrator of the latter (Ceres) was weak. EB12-2 and EB12-3 performed within 24 hours were also scaled together adopting the flux scale of the latter, because the flux calibrator of the former (Ceres) was weak.

The variance of the J1337–1257 flux density listed in Table 1 is much larger than the errors quoted in individual execution blocks, suggesting the presence of underlying systematics of the absolute flux scale as well as potential time variability of J1337–1257 itself. For 11 execution blocks excluding EB7-9 and EB12-2 (for which the flux scale was replaced with those of other execution blocks as mentioned above), the standard deviation of the J1337–1257 flux density at 92 GHz relative to the mean is 5.7%. If we separate the data taken in August, 2014, and the others, it is 3.8%, and 5.7%, respectively, in each data set. If we separate the data taken by the 7-m array and the 12-m array, it is 6.0%, and 4.9%, respectively. Finally, in each of the four spectral windows for the 11 execution blocks, it is 5.7, 6.4, 5.6, 5.7% at 85, 87, 97, 99 GHz, respectively. These values correspond to the variance of the flux scales determined by a range of calibrators used, both solar system objects and J1337–1257. Given these results, we estimate the flux calibration error in the present analysis to be 6%, apart from any unknown systematics that may offset the entire calibration measurements. This precision is consistent with the expected performance of Cycle 2 described in the ALMA Technical Handbook².

¹ <https://almascience.nao.ac.jp/sc/>

² <https://almascience.nrao.edu/documents-and-tools/cycle4/alma-technical-handbook>

3 Imaging Analysis

We performed imaging analysis using CASA version 4.5.0 on the visibility data produced by the ALMA QA2 process. Visibility weights are assigned according to the standard calibration procedure described in Section 2 using CASA versions 4.3.1 and 4.2.2 for the data taken by the 12-m array and the 7-m array, respectively. Natural weighting is adopted to maximize sensitivity to an extended signal. We use the multi-frequency synthesis mode for spectral gridding and the mosaic mode for imaging. Deconvolution is done using the Multi-Scale CLEAN algorithm (see Section 3.3 for details). All the results presented have been corrected for primary beam attenuation. Whenever smoothing is done, a Gaussian kernel is used and the referred size corresponds to FWHM.

3.1 Dirty Maps

Figure 1 shows dirty maps produced directly from the calibrated visibility data for each of the 12-m array and the 7-m array. The synthesized beam parameters are listed in Table 2. The pixel size is $0.5''$. A positive compact source is present near the field center. This source is a known AGN hosted in the Brightest Central Galaxy of RX J1347.5–1145 and its flux density has been reported at a wide range of frequencies in literature (see Figure 1 of Sayers et al. 2016 for a compiled spectrum and references). The baseline coverage of ALMA allows us to identify the position and the flux density of this source almost simultaneously with the SZE, minimizing the impact of source variability and potential systematics of using external datasets. No other compact sources are detected at more than the 4σ statistical significance in the observing field. We present full details of the source subtraction procedure as well as the flux limit on another known radio source in the field in Section 3.2.

Once the compact central source is removed, the extended negative signal of the SZE becomes more apparent. Figure 2 further illustrates that the dynamic range of the signal is enhanced significantly once the data taken by the 12-m array and the 7-m array are combined. The synthesized beam of the combined map has $4.1'' \times 2.5''$ FWHMs with a position angle 84.1° . Positive-valued pixels surrounding the central decrement are due to side-lobes of the dirty beam, which will be corrected by deconvolution in Section 3.3.

To measure the noise levels excluding the extended signal, we also created a difference map by dividing the data set in half, taking a difference between their dirty images, and dividing it by 2 to correct for the reduction of the integration time (right panel of Figure 2). The rms values on the difference map are 0.011, 0.010, 0.012, 0.015, and 0.023 mJy/beam within diameters of 30, 60, 90, 120, and $150''$ around the field center, respectively; the noise level is nearly constant except at the map edge. We have repeated a similar analysis on the 12-m array data and the 7-m array data separately to find that the rms values within the diameter of $90''$ are 0.012 mJy/beam, and 0.083 mJy/beam, respectively.

3.2 Point Source Subtraction

We determined the position and the flux density of the central AGN at our observing bands using long baseline data at the uv distance larger than $30k\lambda$. This cutoff uv distance was chosen to fully separate the compact source from the extended signal beyond $\sim 5''$ as well as to retain an ample signal-to-noise ratio. The source is consistent with a point source if an image was created from visibilities above this cutoff.

Given simplicity of the source shape, we fitted a point source model to the uv data from the central pointing (without mosaicing) varying both the flux density and the position. To examine the spectrum of the source, we performed the fit separately in 84–88 GHz and 96–100 GHz, i.e., in upper and lower two spectral windows. Fitting the data in EB12-1, EB12-2, EB12-3, and EB12-4 simultaneously, we find $F_\nu = 4.16 \pm 0.03 \pm 0.25$ mJy and $3.96 \pm 0.03 \pm 0.24$ mJy at the central frequencies of 86 GHz and 98 GHz, respectively. The first errors are statistical and the second ones are systematic errors from the flux calibration. The best-fit source position is $(13^{\text{h}}47^{\text{m}}30^{\text{s}}.62, -11^{\text{d}}45^{\text{m}}09.5)$ at both frequencies with a statistical error of less than $0.02''$. The spectral index of the source inferred from the two measurements over a narrow range between 86 GHz and 98 GHz is -0.38 ± 0.12 . If the fit is performed for smaller spectral bins, the flux density changes only within the statistical errors. This is also consistent with the spectral index inferred above; the flux density is expected to change by less than about 1% over the frequency difference of 2 GHz in our observing band. We hence did not subdivide the frequency bins further. The best-fit point source models described above were subtracted from the visibility data taken by the 12-m array and the 7-m array, separately in each of the spectral windows covering 84–88 GHz and 96–100 GHz.

When we fit each of EB12-1, EB12-2, EB12-3, and EB12-4 separately, we find that the best-fit flux of the central AGN varies around the above mentioned values by $\pm 4.3\%$ and $\pm 6.4\%$ at 86 GHz and 98 GHz, respectively, whereas the statistical errors are about $\pm 1.5\%$. The variation is correlated with that of the J1337–1257 flux listed in Table 1; the linear correlation coefficients are 0.993 and 0.999, respectively. This suggests that systematic uncertainty of the central AGN flux is indeed dominated by the

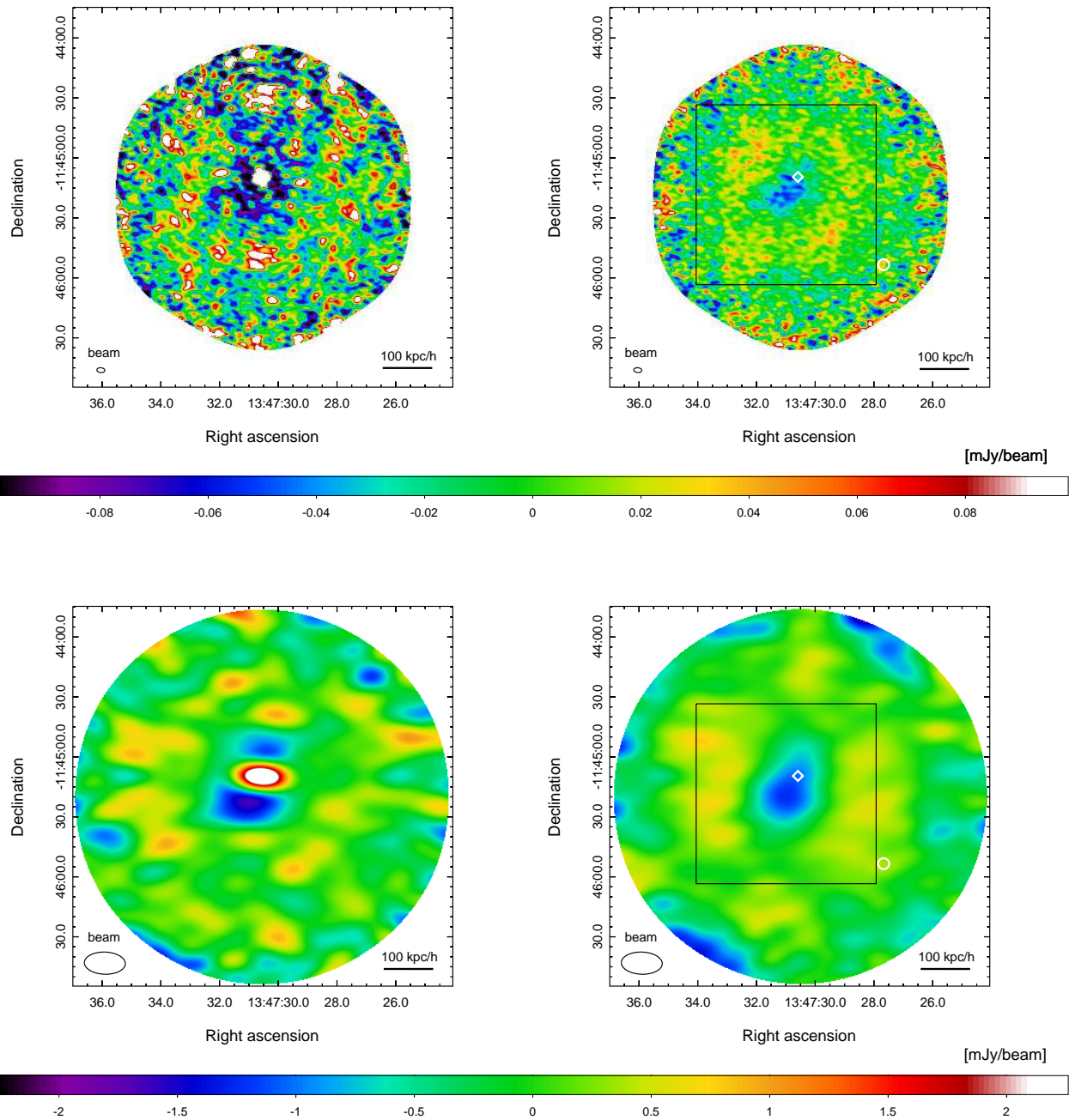


Fig. 1. Dirty maps of the data taken by the 12-m array (top) and the 7-m array (bottom) before (left) and after (right) the central AGN is subtracted. The synthesized beams have $4.1'' \times 2.4''$ FWHMs with a position angle 84.1° and $20.5'' \times 11.1''$ with a position angle 88.1° in the top and bottom panels, as indicated at the bottom left of each panel. In the right panels, the positions of the central AGN (subtracted) and another radio source detected by VLA and SCUBA (unsubtracted and excluded from the analysis) are marked by a diamond and a circle, respectively. The square indicates a $90'' \times 90''$ box centered on the SZE peak over which Figures 2 and 4 are plotted. The ranges of the color scale in all the panels correspond to the same brightness in units of $\text{Jy}/\text{arcsec}^2$.

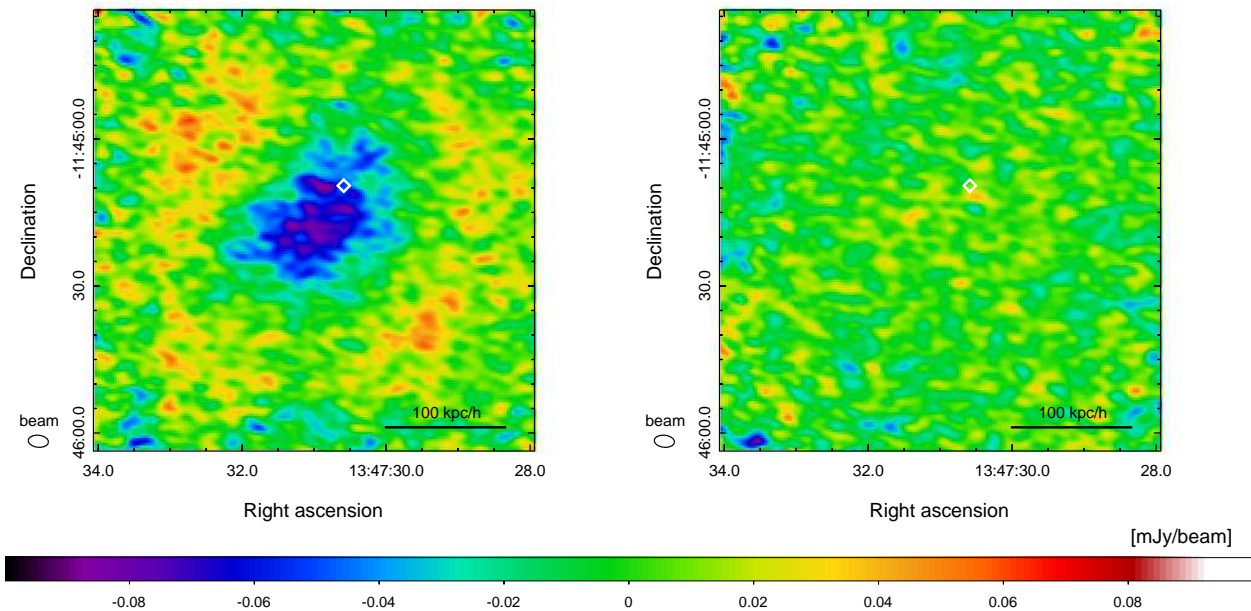


Fig. 2. Dirty map of RX J1347.5–1145 after the central AGN is subtracted and the data taken by the 12-m array and the 7-m array are combined (left). For reference, a difference map created by dividing the data set in half is also shown (right). The position of the subtracted central AGN is marked by a diamond. The synthesized beam has $4.1'' \times 2.5''$ FWHMs with a position angle 84.1° as indicated at the bottom left of each panel. The ranges of the color scale correspond to the same brightness in units of Jy/arcsec² as in Figure 1.

calibration error.

To test consistency of the normalization of the 7-m and 12-m array data, we fitted a point source model to the visibilities taken by the 7-m array between 7 and 16 k λ , the longest uv distances covered by this array. Given poorer statistics of the 7-m array data, all the spectral windows between 84 GHz and 100 GHz are fitted together fixing the source coordinate at the best-fit position from the 12-m array data. From the data in all the execution blocks for the 7-m array, the fitted value of the AGN flux density is $4.09 \pm 0.17 \pm 0.25$ mJy. If we separate the data taken in 2014 August and 2014 December, they are $4.22 \pm 0.24 \pm 0.25$ mJy and $3.95 \pm 0.24 \pm 0.24$ mJy, respectively. Statistical errors are too large to examine a correlation with the J1337–1257 flux density for the 7-m array. For comparison, a similar fit to the 12-m array data between 7 and 16 k λ yields $4.04 \pm 0.03 \pm 0.24$ mJy. The flux values measured by the two arrays are thus consistent within the statistical and calibration errors.

In addition to the calibration error of 6% on the total SZE flux, the intensity of the source-subtracted map is subject to a position-dependent error from the adopted source flux. At the subtracted source position, this error is estimated to be at most 3% of the source flux (~ 4 mJy), i.e., 0.12 mJy/beam, after the data from 4 and 9 execution blocks are combined for the 12-m array and the 7-m array, respectively. The error becomes smaller than the noise level of 0.012 mJy/beam at 2.9'' away from the source for an average beam FWHM of 3.2'' in the present case.

Note that the flux density of the central AGN measured by ALMA in 2014 December and 2015 January are lower than 4.9 ± 0.1 mJy measured by the 23 element array of CARMA in 2011 February at the central frequency of 86 GHz (Plagge et al. 2013); the fitted source position is in good agreement with that of CARMA. A part of the difference may be ascribed to a long-term variability of the AGN over nearly four-year period as well as to calibration between ALMA and CARMA. Even if we further allow for an additional bias of +1 mJy for the central source flux, the biased intensity in the source-subtracted map drops below the noise level at 4.0'' away from the source.

We hence conclude that the flux calibration error hardly affects *morphology* of the source-subtracted map except in the vicinity of the source position. Still, its impact on the total flux should be treated with care.

There is another known radio source in the field of RX J1347.5–1145 at ($13^{\text{h}}47^{\text{m}}27^{\text{s}}.7, -11^{\text{d}}45^{\text{m}}53.4$) with the 1.4 GHz flux density of 4.50 ± 0.06 mJy measured by VLA (Gitti et al. 2007) and the 350 GHz flux density of 15.4 ± 5.3 mJy measured by SCUBA (Kitayama et al. 2004). This source is located at $\sim 60''$ away from the central AGN (a circle in Figure 1). Being at the map edge, this source is not clearly detected in the present ALMA data while there is a hint of a positive signal at about the 3σ statistical

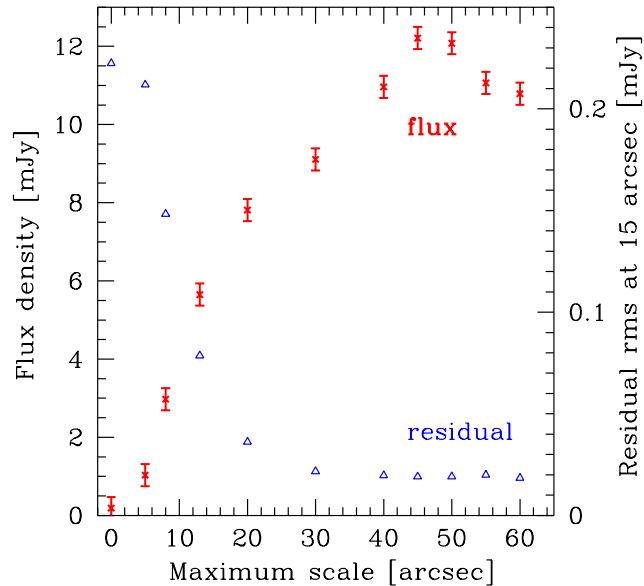


Fig. 3. Recovered flux and residuals of deconvolved images versus the maximum scale of Gaussians used in Multi-Scale CLEAN. Wherever smaller than the scale shown in the figure, Gaussians with FWHMs of 0, 5'', 8'', 13'', 20'', and 30'' are also used in the deconvolution, i.e., the smaller scale values are fixed for comparison. The plotted residual is the rms value measured on a residual map after being corrected for primary beam attenuation and smoothed with a Gaussian kernel to a fixed resolution of 15'' FWHM. Both flux and residuals are measured within a diameter of 90'' around the field center.

significance. The 92 GHz flux density measured within the diameter of 10'' around the reported VLA position is 0.17 ± 0.06 mJy. We do not subtract this source and simply exclude its position from the analysis presented in this paper.

3.3 Deconvolution of Extended Signal

To correct for incomplete sampling of the visibility data, we performed image deconvolution using the Multi-Scale CLEAN algorithm implemented in CASA. This method models an image by a sum of Gaussians of various sizes and is shown to recover much higher fraction of flux for extended sources than the conventional CLEAN algorithm (Cornwell 2008; Rich et al. 2008). It also has an advantage over the Maximum Entropy Method (e.g., Narayan & Nityananda 1986; Sault 1990) in that it is free from the positivity constraint.

There are some free parameters in Multi-Scale CLEAN, such as the sizes of Gaussian components used for deconvolution and the scale bias parameter by which residuals at different scales are weighted (Cornwell 2008). Optimal choices of these parameters depend on the target and the instrument in consideration. Having searched for a combination of parameters that gives minimal residuals as well as the maximal recovered flux, we adopt the scales [0, 5'', 8'', 13'', 20'', 30'', 45''] with the small-scale bias parameter of 0.4 as our fiducial choice. The scale 0 corresponds to the size of a synthesized beam, i.e., the scale used in the conventional (single-scale) CLEAN algorithm. We also use a loop gain of 0.05 suitable for diffuse emission and a flux threshold of 0.03 mJy (2.5σ); the flux threshold is reached by less than 10,000 iterations in all the cases presented in this paper.

Figure 3 illustrates how the recovered flux and residuals change as we successively add a larger scale in the deconvolution. To examine the sensitivity to an extended signal, the residual maps are smoothed by a Gaussian kernel to a resolution of 15'' FWHM and the rms values within a diameter of 90'' around the field center are plotted. They are compared with the flux within the same region of the deconvolved image. Converged results are obtained by taking the largest scale to be between 40'' and 50'', corresponding to the maximum recoverable scale for the shortest baseline length of 2.1 k λ in the present data. We have also checked that the deconvolved results are insensitive to the value of the small-scale bias parameter as long as its value is less than 0.8.

While the above procedure gives robust reconstruction of the observed signal up to a spatial scale of $\sim 40''$, flux at larger scale is still lost in currently available ALMA data with no total power measurements. In what follows, we focus on the results that can be derived solely at $< 40''$ and discuss separately the degree of missing flux by means of simulations in Section 4.2.

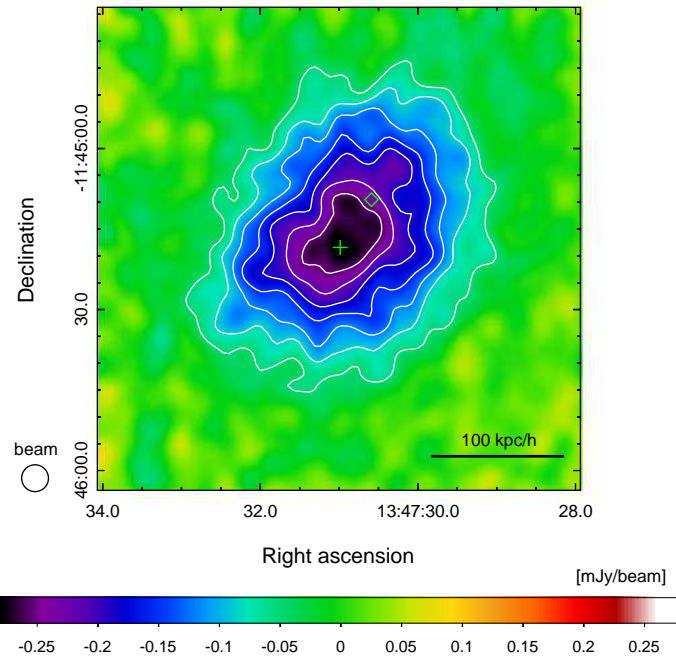


Fig. 4. Deconvolved map of RX J1347.5–1145 by ALMA at the central frequency of 92 GHz smoothed to have a symmetrical beam with $5''$ FWHM. Contours show 3, 5, 7, 9, 11, 13, 15σ statistical significance levels with $1\sigma = 0.017$ mJy/beam. The positions of the SZE peak and the subtracted central AGN are marked by a cross and a diamond, respectively.

3.4 The Sunyaev-Zel'dovich Effect Map of RX J1347.5–1145

Figure 4 shows the deconvolved map smoothed to an effective beam size of $5''$ FWHM. Asymmetry of the synthesized beam has been corrected, to study morphology of the emission. Applying the same smoothing to the difference map shown in the right panel of Figure 2, we measure the rms noise level of 0.017 mJy/beam over a diameter of $90''$ around the field center. As described in Section 3.2, the rms values are nearly constant within this diameter. We hence adopt 0.017 mJy/beam when denoting the statistical significance within the same region of the smoothed image.

To examine characteristics of the signal and noise, we plot in Figure 5 the absolute magnitude (root sum square of real and imaginary parts) of the Fourier transform of the deconvolved SZE map and the difference map. Note that the plotted quantities are different from observed visibilities. The Fourier transform was applied to the unsmoothed maps over a square box of $90'' \times 90''$ around the peak of the decrement. The deconvolved map is dominated by an extended signal over noise at $\gtrsim 15''$. As mentioned in Section 3.3 and will be tested further using simulations in Section 4.2, the extended signal up to the spatial scale of about $40''$ is recovered in the current deconvolved map, whereas the flux at a larger scale is lost owing to lack of the shorter spacing data.

In Figure 4, the decrement signal from the SZE is detected at more than 15σ statistical significance with $5''$ resolution; its peak position ($13^{\text{h}}47^{\text{m}}31^{\text{s}}.02, -11^{\text{d}}45^{\text{m}}18.4$) is at $11''$ to the south-east from the central AGN. A separation of $11''$ is more than 8σ away for the synthesized beam of ALMA and the uncertainty of the AGN flux does not affect the intensity of the south-east peak nor overall morphology of the image. The measured intensities at the south-east peak and at the AGN position are $-0.286 \pm 0.017 \pm 0.017$ mJy/beam and $-0.234 \pm 0.017 \pm 0.12$ mJy/beam, respectively (quoted systematic errors are from the flux calibration and the source subtraction). There is also a weak local peak with $-0.221 \pm 0.017 \pm 0.013$ mJy/beam at $7''$ to the north-west of the central AGN. The measured flux within a radius of $40''$ from the south-east peak is $-12.4 \pm 0.2 \pm 0.8$ mJy. The mean signal within the annulus at $40'' - 45''$ from the south-east peak is consistent with zero and 0.0004 ± 0.0010 mJy/beam.

We present in Figure 6 azimuthally averaged intensity profiles as a function of the distance from the central AGN position. Unsmoothed pixel data are binned and the statistical error of the mean in each bin is computed by

$$\sigma_{\text{bin}} = \frac{1}{\sqrt{N_{\text{beam}}}} \max(\sigma_{\text{std}}, \sigma_{\text{map}}), \quad (1)$$

where σ_{std} is the standard deviation of the pixel data in the bin, σ_{map} is the map noise, and N_{beam} is the number of independent

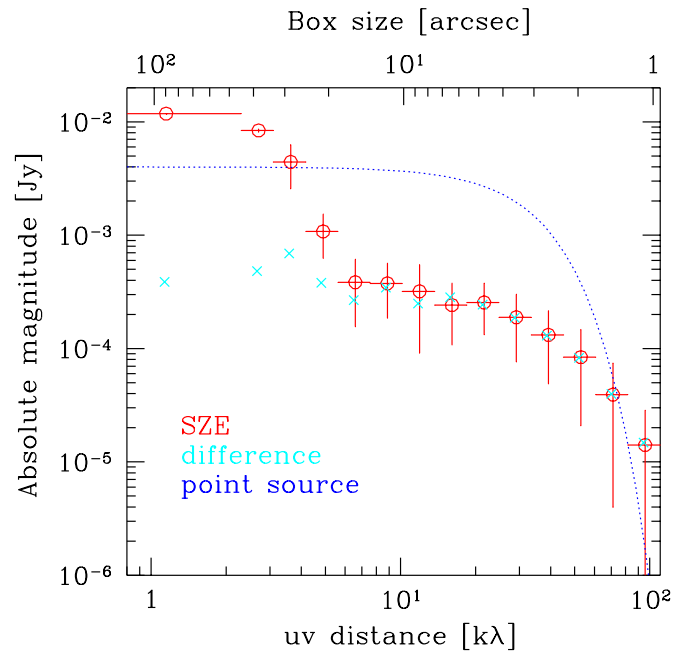


Fig. 5. Absolute magnitude of the Fourier transform of the deconvolved SZE map (circles) and the difference map in the right panel of Figure 2 (crosses). Vertical error bars indicate standard deviations of the absolute magnitude in each bin. Also plotted for reference is the magnitude for a 4 mJy point source convolved with a Gaussian beam with the average FWHM of $3.2''$ (dashed line). The top axis shows the box size over which the data are sampled on the image. For clarity, symbols have been slightly shifted horizontally.

beams in the bin (we use N_{beam} instead of the number of pixels, because the pixel values in a deconvolved image are correlated within the beam area). The calibration error of 6% is then added in quadrature to the error in each bin. To illustrate the impact of the systematic error of the subtracted AGN flux, we plot in the same figure the azimuthally averaged shape of the dirty beam (the point spread function before sidelobes are corrected) normalized to have the peak value corresponding to 0.12 mJy/beam in the unsmoothed map. Only the central bin may potentially be affected by the error of the subtracted AGN flux.

Figure 6 shows that the intensity in the south-east quadrant is significantly stronger, whereas extended signals are present in all the quadrants. The average signal excluding the south-east quadrant drops to zero at $38''$ from the central AGN. For reference, we also plot a spherically symmetric SZE model based on the Chandra X-ray data of this cluster excluding the south-east quadrant. Spatially resolved and deprojected electron temperatures are taken from Table 7 of Ota et al. (2008) with the relativistic correction of the SZE by Nozawa, Itoh & Kohyama (2005) at 92 GHz; the radial electron density profile is modeled by a sum of two β -models (Cavaliere & Fusco-Femiano 1978), $n_e(r) = n_{e1}[1 + (r/r_{c1})^2]^{-3\beta/2} + n_{e2}[1 + (r/r_{c2})^2]^{-3\beta/2}$, with the parameters obtained from fitting the X-ray brightness at 0.4–7.0 keV, $n_{e1} = (0.241 \pm 0.007) h^{1/2} \text{cm}^{-3}$, $r_{c1} = (9.14 \pm 0.74) h^{-1} \text{kpc}$, $n_{e2} = (0.055 \pm 0.008) h^{1/2} \text{cm}^{-3}$, $r_{c2} = (36.6 \pm 2.7) h^{-1} \text{kpc}$, and $\beta = 0.568 \pm 0.004$; the projected SZE intensity is convolved with the synthesized beam of ALMA; and the zero-brightness level is taken at $38''$ from the central AGN (the AGN lies less than $1''$ from the X-ray peak). Note that the spherical model SZE profile varies as $\propto h^{-1/2}$ and $h = 0.7$ is assumed for definiteness in Figure 6. The signal in the south-east quadrant is clearly stronger than the other quadrants. The average intensity profile excluding the south-east quadrant is in broad agreement with the spherical model, although it tends to be weaker by $\sim 10\%$. The difference may be ascribed to the kinematic SZE, asphericity of the cluster, the missing flux of the ALMA map, the calibration error of ALMA (Section 2) or Chandra (Reese et al. 2010), a higher value of h , or any combination thereof. Regarding the first possibility, the peculiar velocity of this cluster $v_{\text{pec}} = -1040_{-840}^{+870} \text{ km/s}$ reported by Sayers et al. (2016) reduces the observed SZE signal at 92 GHz by $8.8_{-7.4}^{+7.1} \%$ for the mean electron temperature of $kT_e = 13 \text{ keV}$ (Ota et al. 2008). We will discuss the second and the third possibilities in detail in Sections 4.1 and 4.2.

The above results demonstrate ALMA's powerful capability of detecting an extended SZE signal. They also confirm, with much improved spatial resolution and sensitivity, the previous findings (Komatsu et al. 2001; Allen et al. 2002) of a substructure in the south-east quadrant of this cluster and identify its location regardless of the presence of the central AGN. Their implications including detailed comparison with the X-ray data as well as with the previous SZE observations of this cluster are presented in the

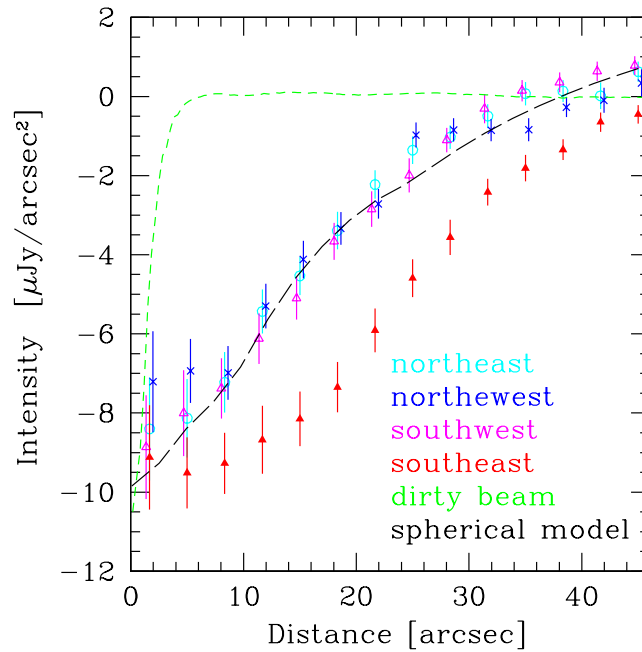


Fig. 6. Azimuthal average of the measured intensity as a function of the distance from the central AGN position in four quadrants; northeast (open circles), northwest (crosses), southwest (open triangles) south east (filled triangles). Error bars indicate statistical and systematic errors of the mean in each bin. For clarity, symbols have been slightly shifted horizontally. For reference, the short dashed line shows the azimuthally averaged shape of the dirty beam normalized to have the peak value of 0.12 mJy/beam in the unsmoothed map. The long dashed line shows the shape of a spherical model profile from the Chandra X-ray data excluding the south-east quadrant with the zero-brightness level taken at the distance of 38'' from the central AGN; the model profile varies as $\propto h^{-1/2}$ and $h = 0.7$ is assumed in the figure.

following sections.

4 Interpretation and Implications

4.1 X-ray Data of RX J1347.5–1145

To perform detailed comparison with the ALMA results (Section 3.4) as well as to construct a realistic model for imaging simulations (Section 4.2), we extracted 6 data sets of RX J1347.5–1145 taken by ACIS-S (ObsID 506 and 507) and ACIS-I (ObsID 3592, 13516, 13999, and 14407) on board Chandra X-ray observatory. After excluding the periods with high background rates, the total net exposure time amounts to 233.8 ks. The data were processed using CIAO version 4.7 (Fruscione et al. 2006) and the Calibration database (CALDB) version 4.6.9. Given that the cluster is highly compact compared to the field-of-view of ACIS, we estimated the backgrounds from the off-center region at 2.5' – 3.5' away from the X-ray peak of this cluster, where the intracluster emission is negligible. Exposure-corrected and background-subtracted data at 0.4–7.0 keV were used throughout our analysis. Spectral fitting was done with XSPEC version 12.9.0o (Arnaud 1996), assuming that the intracluster plasma is in collisional ionization equilibrium and the metal abundance ratio is that of Anders & Grevesse (1989). The source redshift and Galactic hydrogen column density were fixed at $z = 0.451$ and $N_{\text{H}} = 4.6 \times 10^{20} \text{ cm}^{-2}$ (Kalberla et al. 2005), respectively.

We performed X-ray thermodynamic mapping using the contour binning algorithm (Sanders 2006) to define sub-regions with nearly equal photon counts. Fitting a spectrum in each sub-region defined by this algorithm yields projected temperature, metallicity, and spectral normalization factor. From these quantities, “pseudo” electron density and pressure were computed assuming that the gas is distributed uniformly over the line-of-sight distance of L . These are not real electron density or pressure maps, as we did not perform any deprojection to estimate a three-dimensional distribution. The pseudo electron density map is essentially the square-root of the projected X-ray intensity ($\propto \int n_e^2 dl$), while the pseudo pressure map is a product of the pseudo density and the projected X-ray temperature. The absolute values of the density and the pressure are arbitrary (both varies as $L^{-1/2}$) and only morphology of the maps is to be compared with the SZE. We adopt the S/N threshold of 83 (~ 7000 counts) to obtain typical statistical errors 5% for the density and 10% for the temperature and the pressure.

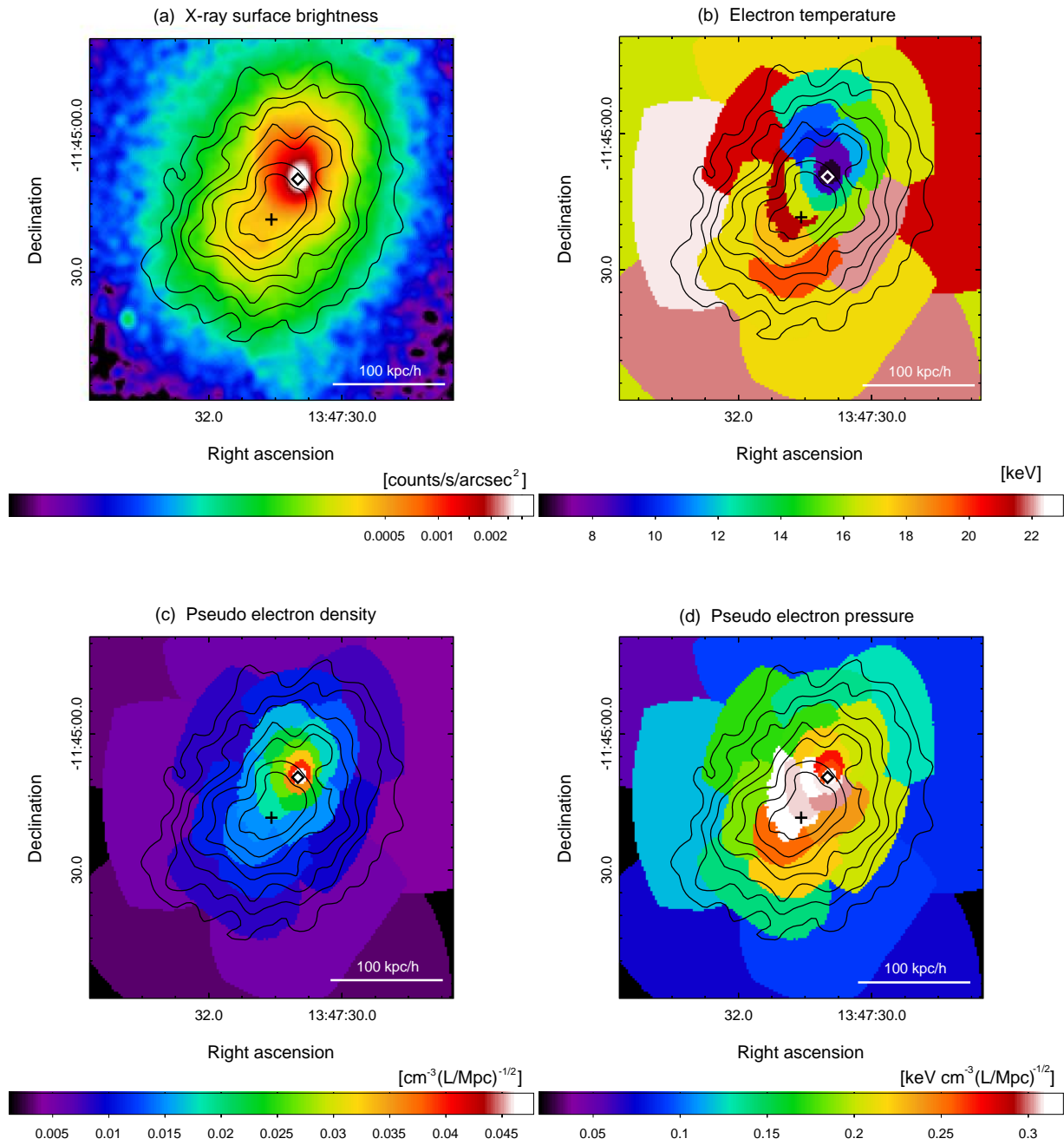


Fig. 7. Comparison of the ALMA SZE data and the Chandra X-ray images of RX J1347.5–1145. In all panels, contours indicate the significance levels of the ALMA SZE map plotted in Figure 4, and a cross and a diamond indicate the positions of the SZE peak and the central AGN, respectively. (a) The X-ray surface brightness at 0.4–7.0 keV in counts/s/arcsec², smoothed by a Gaussian kernel with 2.3'' FWHM. (b) Projected X-ray spectroscopic temperature in keV, based on the contour binning algorithm (Sanders 2006) with the S/N threshold of 83 (7000 counts) per region. (c) Pseudo electron density map in cm⁻³(L/Mpc)^{-1/2} assuming a uniform line-of-sight depth of L . (d) Pseudo electron pressure map in keV cm⁻³(L/Mpc)^{-1/2}, a product of quantities plotted in panels (b) and (c).

Figure 7 compares the X-ray measured quantities with the ALMA SZE contours. The pseudo pressure map (panel d) shows a reasonable agreement with the ALMA SZE map, including the south-east peak position and elongated structure of the emission. The projected mean temperature (panel b) exceeds 20 keV around the SZE peak in accord with the results of Kitayama et al. (2004) and Ota et al. (2008). While departure from spherical symmetry is indicated in all the maps, disturbance is more obvious in the SZE, temperature, and pressure maps than in the X-ray brightness or density maps. Being proportional to the density squared, the X-ray brightness tends to peak sharply within the central cool core. The spatial resolution of the ALMA map ($20 h^{-1}$ kpc) allows us to clearly separate the cool core and the south-east pressure peak.

The position of the central AGN identified in the ALMA data agrees with the X-ray peak to within $1''$. The central AGN is faint in X-rays with an upper limit (1σ) on the 2–10 keV luminosity of 4.38×10^{42} ergs/s.

4.2 Imaging Simulations: How Much Flux is Missing on Large Scales?

Given good agreement between the ALMA map and the X-ray inferred pressure map derived in the previous section, we performed imaging simulations using the latter as a realistic input model to quantify the degree of missing flux for RX J1347.5–1145. The absolute value of the pressure was normalized so that the peak value corresponds to the Compton y -parameter of $y_{\text{peak}} = 8 \times 10^{-4}$ as inferred from the previous SZE measurements of this cluster (Komatsu et al. 2001; Kitayama et al. 2004). A relativistic correction to the SZE intensity by Nozawa, Itoh & Kohyama (2005) was applied adopting the projected temperature shown in Figure 7(b) at each sky position.

We created model images separately at four spectral windows centered at 85, 87, 97, and 99 GHz with an effective bandwidth of 1.875 GHz each. The pointing directions, the array configuration, the hour angle, the total effective integration time, and the average perceptible water vapour were set to match those of each executing block of real observations. Visibility data were then produced using the CASA task *simobserve*. Three sets of the data were produced and used for different purposes; (1) visibility without signal but includes instrumental and atmospheric noise expected for ALMA in each spectral window, (2) visibility without noise but includes signal, and (3) visibility with both noise and signal. The rms levels of dirty images created from the first set of visibility were consistent with the values given in Section 3.2. The second and the third sets of visibility were deconvolved in the same way as the real data as described in Section 3.3. In the following, the simulation results are compared with the input signal at the central frequency 92 GHz, to take account of any bias arising from spectral bandpass of the observations and the data analysis.

Figure 8 compares the simulated ALMA maps to the input; note that the range of the color scale of panel (a) is wider than that of panels (b)–(d). The amplitude of the Fourier transform of each map is plotted in Figure 9. The simulated signal and noise both show similar magnitude to the real data plotted in Figure 5. A large fraction ($\sim 80\%$) of flux is lost at the smallest uv distance, whereas reconstruction becomes accurate at $2.5 - 20$ k λ , corresponding to the spatial size of $40'' - 5''$. At larger uv distances, reconstruction is limited by noise and finite spatial resolution. These results suggest that the amount of the missing flux is controlled primarily by the uv coverage and the deconvolution method. An azimuthally-averaged amplitude at a fixed uv distance intrinsically has a large dispersion owing to asymmetry of the emission. In the following, we present two different approaches to model the amount of the missing flux.

The first approach (hereafter correction (i)) is to correct the intrinsic signal in Fourier space. The right panel of Figure 9 shows the ratio of the amplitude of simulated signal (without noise) to that of the input map. Apart from the dispersion arising from asymmetry of the emission, the average ratio is well described by a product of a large-scale fall-off factor (solid line) obtained by interpolating the points at the shortest uv distances, and a Gaussian clean beam (dashed line) that accounts for a finite angular resolution of the image. A correction is then applied by multiplying these two factors to the Fourier transform of the input model at 92 GHz; in practice, the latter factor was applied equivalently as a convolution with a Gaussian kernel in real space. Figures 10(a) and (b) show that correction (i) reproduces well the simulated map with both signal and noise; the residual is consistent with noise plotted in Figure 8(d).

The second approach (hereafter correction (ii)) relates the input and output maps directly in real space. Figure 11(a) compares the intensity of the output map from the simulation with both signal and noise I_{ν}^{out} to that of the input map I_{ν}^{in} (error bars), both smoothed to the beam size of $5''$ FWHM. A set of data ($I_{\nu}^{\text{out}}, I_{\nu}^{\text{in}}$) was created for each sky position and then binned in an ascending order of I_{ν}^{in} ; the error bars on I_{ν}^{out} and I_{ν}^{in} in Figure 11 indicate standard deviations in each bin. For comparison, the same binning procedure was repeated by replacing I_{ν}^{out} with the intensity of the simulated map with only signal (triangles) as well as the input map to which correction (i) is applied (circles). A tight correlation is found among these quantities. The dashed line in Figure 11 indicates a linear approximation to this correlation obtained from a fit to the *unbinned* set of ($I_{\nu}^{\text{out}}, I_{\nu}^{\text{in}}$):

$$I_{\nu}^{\text{out}} = c_1 I_{\nu}^{\text{in}} + c_0 \quad (2)$$

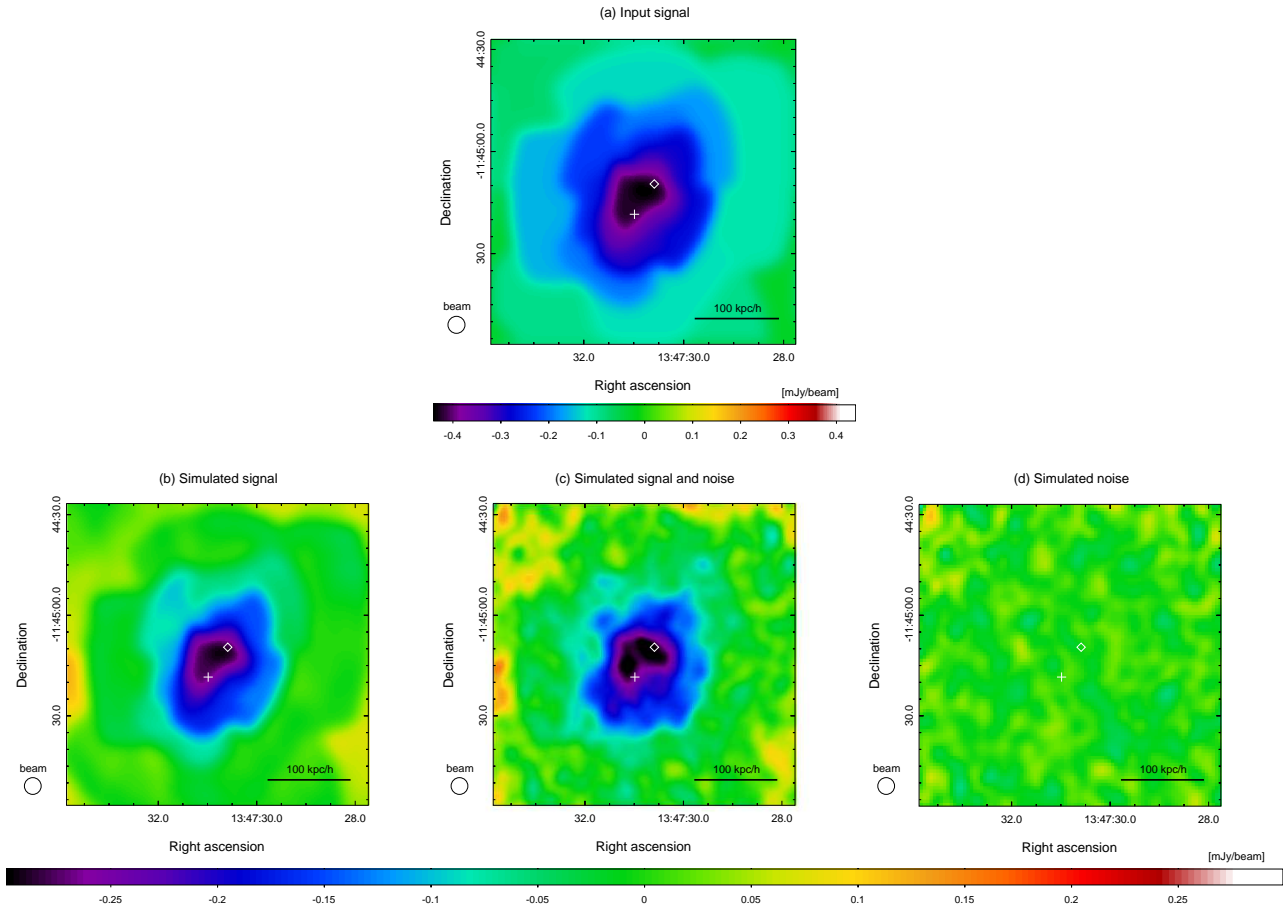


Fig. 8. Mock ALMA SZE maps of RX J1347.5–1145 with $y_{\text{peak}} = 8 \times 10^{-4}$. (a) Input map at 92 GHz. (b) Simulated map with signal only. (c) Simulated map with both signal and noise. (d) Simulated map with noise alone; the rms value over the plotted region is $20 \mu\text{Jy/beam}$. All the maps have been smoothed to the resolution of $5''$ FWHM and have the size $90'' \times 90''$ centered at the emission peak of the input map. For reference, the positions of the central AGN and the SZE peak in the *observed* ALMA map are marked by a diamond and a cross, respectively.

with $c_1 = 0.88$ and $c_0 = 3.6 \mu\text{Jy/arcsec}^2$. The root-mean-square deviation of the unbinned set of $(I_\nu^{\text{out}}, I_\nu^{\text{in}})$ from the best-fit relation is $\Delta I_\nu^{\text{in}} = 0.88 \mu\text{Jy/arcsec}^2$; we will adopt $\sqrt{2}$ times this value ($\Delta I_\nu^{\text{in}} = 1.3 \mu\text{Jy/arcsec}^2$) as the 1σ error of the relation when a constant offset (c_0) is subtracted later in our analysis. Correcting the input model using equation (2) also gives a good match to the simulated map with both signal and noise (Figures 10 c,d) and is consistent with the results of correction (i) (Figure 11a).

To test robustness of correction (ii), we repeated the simulations by doubling or halving the signal of the entire input map to have $y_{\text{peak}} = 16 \times 10^{-4}$ or 4×10^{-4} , and adopting different noise realizations. A similar relation was found between I_ν^{out} and I_ν^{in} but with different values of c_0 ; they converge on a single relation within the range of quoted uncertainties ($\Delta I_\nu^{\text{in}} = \pm 1.3 \mu\text{Jy/arcsec}^2$) once the offset of the zero brightness level is removed as plotted in the right panel of Figure 11. A physical reason for self-similarity of the relation is that multiplying the large-scale fall-off factor in Fourier space is equivalent to subtracting the signal convolved with a corresponding kernel function in real space, which leaves nearly a constant fraction of the original signal on the deconvolved map. The specific form of the relation depends on the source shape and the observing configuration.

The above results imply that the intensity measured on the observed ALMA map of RX J1347.5–1145 provides a reasonable representation of *differential* values of the true intensity. The missing flux primarily resides in a constant offset of the entire map. An additional reduction factor of 12% (c_1 in equation [2]) and its uncertainty $\Delta I_\nu^{\text{in}} = \pm 1.3 \mu\text{Jy/arcsec}^2$ (including the error of subtracting c_0 in equation [2]) should also be taken into account when the measured intensity is converted to the intrinsic intensity using correction (ii).

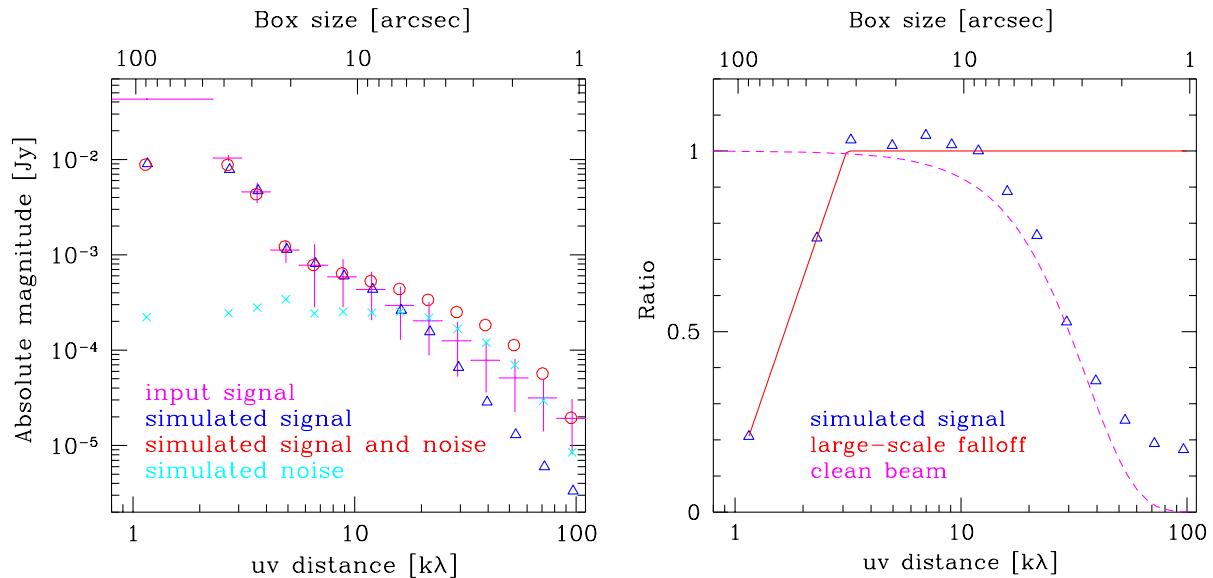


Fig. 9. Fourier transform of mock ALMA maps. *Left:* Absolute magnitude of the input map at 92 GHz before observed by ALMA (error bars), simulated ALMA map with signal only (triangles), simulated ALMA map with both signal and noise (circles), and simulated ALMA map with noise alone (crosses). Vertical error bars indicate standard deviations of the absolute magnitude in each bin. For clarity, they are plotted only for the input map and those of the simulated map with signal and noise are similar to those of the observed map plotted in Figure 5. Symbols have been slightly shifted horizontally for display. *Right:* Ratio of the absolute magnitude of the Fourier transform of the simulated signal without noise to that of the input map (triangles), the factor to model a falloff at large spatial scales (solid line), and a Gaussian clean beam to account for finite spatial resolution (dashed line). The top axis shows the box size over which the data are sampled on the image.

4.3 Differential y -parameter map

We use the results of simulations presented in Section 4.2 to bridge between the observed ALMA map and the intrinsic signal of RX J1347.5–1145. Figure 12 shows the Compton y -parameter map reconstructed from the observed ALMA map in Figure 4. The plotted values correspond to *differential* y -parameter (Δy) with respect to the positions at $40''$ from the SZE intensity peak. The relativistic correction by Nozawa, Itoh & Kohyama (2005) has been applied assuming the projected temperature shown in Figure 7(b) at each sky position. The missing flux has been modeled by correction (ii) described in Section 4.2; the map is divided by the mean reduction factor of 0.88 (c_1 in equation [2]) and the mean value at $40''$ from the emission peak $\Delta y = (8.6 \pm 3.5) \times 10^{-6}$ is subtracted from the entire map to define the zero level.

The peak value of the Compton y -parameter is $\Delta y = (5.9 \pm 0.4 \pm 0.8) \times 10^{-4}$ relative to the positions at $40''$ away from the peak. Similarly, an integrated flux measured within the radius $40''$ from the peak corresponds to $\Delta Y = \int \Delta y d\Omega = (1.6 \pm 0.03 \pm 0.8) \times 10^{-11}$. In both cases, quoted systematic errors are from the missing flux correction ($1.3 \mu\text{Jy}/\text{arcsec}^2$) and the flux calibration (6%). If present, the peculiar motion of the cluster along the line-of-sight changes the above values further by $\sim 8\%$ $[v_{\text{pec}}/(1000 \text{ km s}^{-1})][kT_e/13 \text{ keV}]^{-1}$ via the kinematic SZE.

4.4 Comparison with Previous SZE Observations

Figure 13 exhibits comparison of the ALMA map with previous SZE observations of RX J1347.5–1145 by MUSTANG (Mason et al. 2010; Korngut et al. 2011) and NOBA (Komatsu et al. 2001). The MUSTANG data shown in this figure are essentially the same as those published in Mason et al. (2010) and Korngut et al. (2011), except that they were processed with an updated pipeline (B. Mason and C. Romero, private communication; Romero et al. 2015). For closer comparison with the MUSTANG data, the deconvolved ALMA map was corrected for the missing flux by dividing by a factor of 0.88 and adding a constant offset; the central AGN with the inferred mean flux of 4.06 mJy at 92 GHz was re-added; the map was smoothed to the same effective resolution as the MUSTANG contours; and the value of the offset is adjusted so that the mean brightness at $40''$ from the SZE peak of the unsmoothed ALMA map (the positions marked by the dashed circles in Figure 13) matches that of the MUSTANG map, $-0.046 \text{ mJy}/\text{beam}$. Note that we only compare the brightness relative to these offset positions.

The NOBA data shown in Figure 13(c) are identical to those of Komatsu et al. (2001). Also for direct comparison with the NOBA

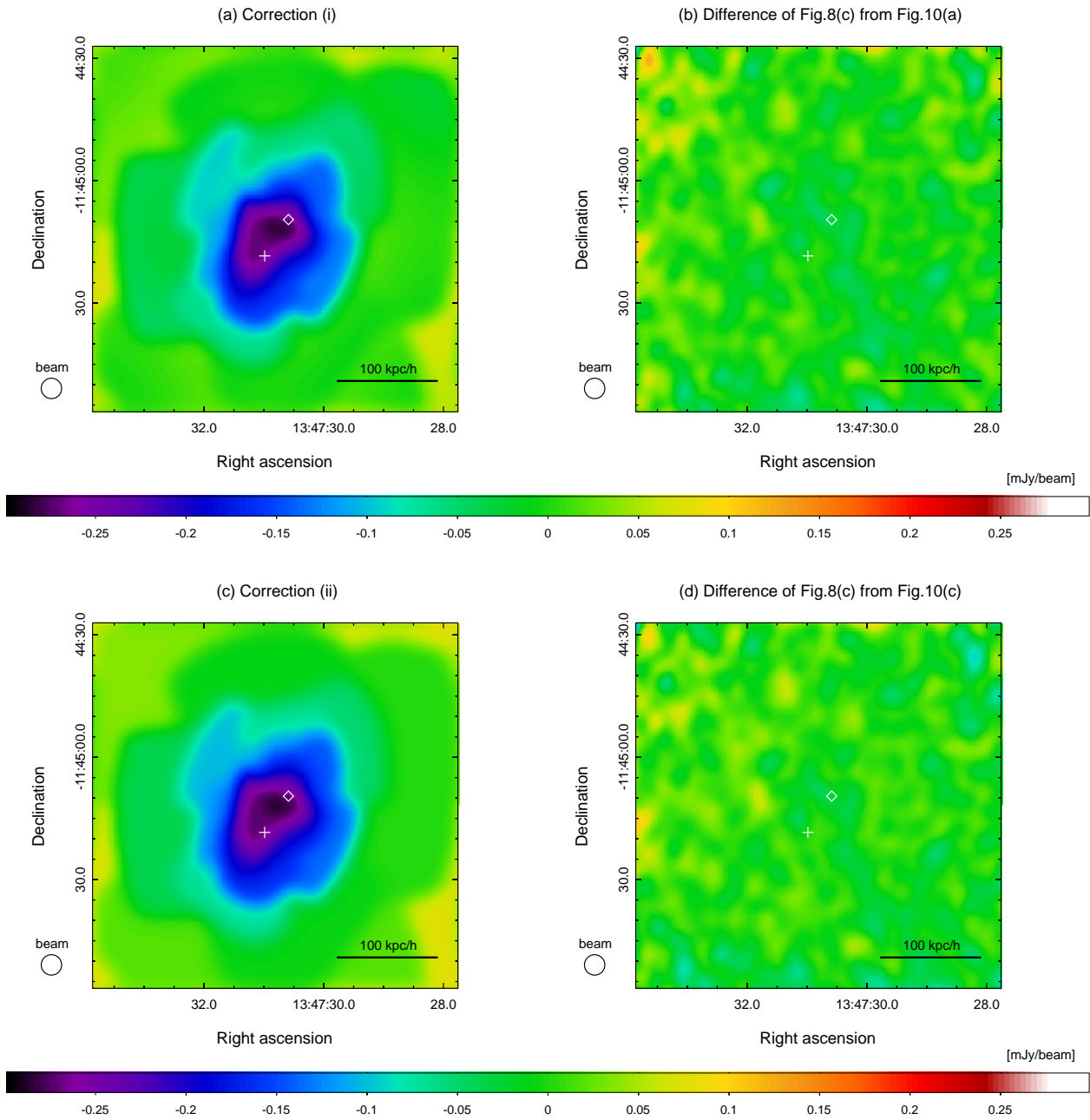


Fig. 10. Model SZE maps of RX J1347.5–1145 with $y_{\text{peak}} = 8 \times 10^{-4}$ corrected for the missing flux of the ALMA observations. (a) Input map to which correction (i) is applied. (b) The difference of Figure 8(c) from Figure 10(a); the rms value of the map is $22 \mu\text{Jy/beam}$. (c) Input model to which correction (ii) is applied using equation (2). (d) The difference of Figure 8(c) from Figure 10(c); the rms value of the map is $22 \mu\text{Jy/beam}$. All the maps have been smoothed to the resolution of $5''$ FWHM and have the size $90'' \times 90''$ centered at the emission peak of the input map. For reference, the positions of the central AGN and the SZE peak in the *observed* ALMA map are marked by a diamond and a cross, respectively. The range of the color scale is the same as Figures 8(b)–(d).

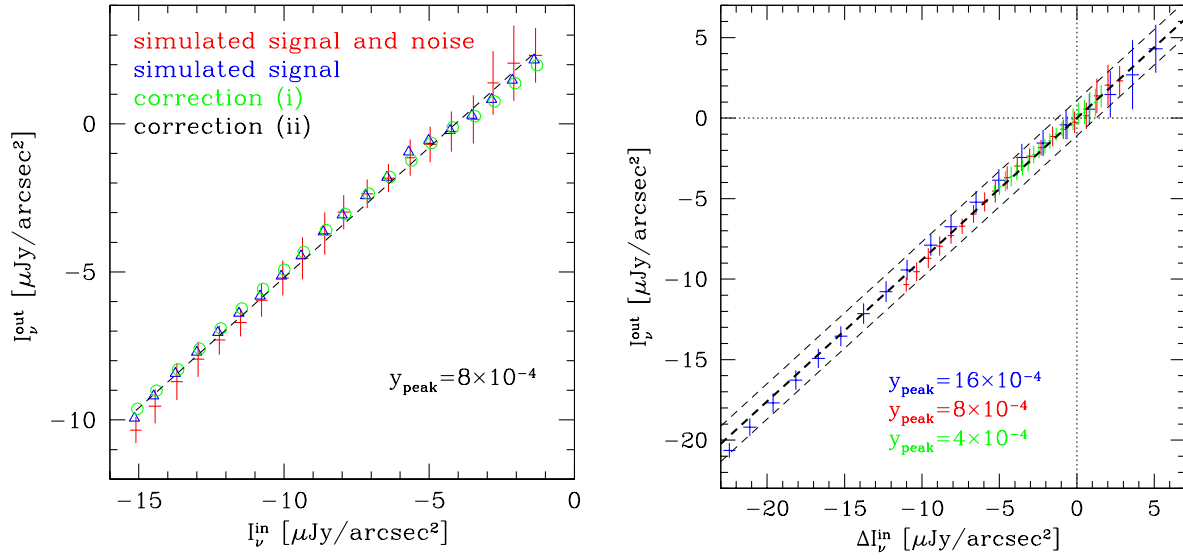


Fig. 11. Relation between the output intensity and the input intensity at 92 GHz from the simulations for RX J1347.5–1145. Horizontal and vertical error bars denote standard deviations in each bin. For clarity, they are plotted only for the simulated map with both signal and noise. *Left:* Error bars indicate the simulation with both signal and noise for $y_{\text{peak}} = 8 \times 10^{-4}$. Also plotted are the simulation with signal only (triangles), the input model to which correction (i) is applied (circles), the input model to which correction (ii) is applied using equation (2) (dashed line). For clarity, symbols have been slightly shifted horizontally. *Right:* Error bars indicate the simulation with both signal and noise for $y_{\text{peak}} = 16 \times 10^{-4}$ (blue), 8×10^{-4} (red), and 4×10^{-4} (green), against the input intensity after a constant offset ($\Delta I_{\nu}^{\text{in}} = +7.8, +4.1, +2.2 \mu\text{Jy}/\text{arcsec}^2$, respectively) is applied to give zero intercept. The thick dashed line shows the relation given by equation (2) but taking $c_0 = 0$, and the thin dashed lines indicate the range of 1σ systematic uncertainties from it ($\Delta I_{\nu}^{\text{in}} = \pm 1.3 \mu\text{Jy}/\text{arcsec}^2$).

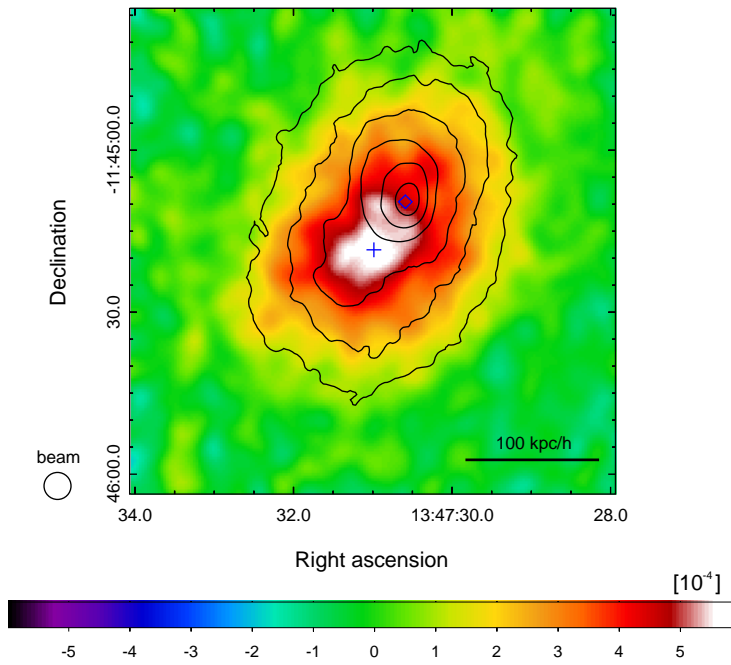


Fig. 12. Differential Compton y -parameter map of RX J1347.5–1145 with $5''$ resolution reconstructed from the observed ALMA SZE map at 92 GHz. The map is corrected for the missing flux and the zero level is taken at $40''$ from the SZE intensity peak position marked by a cross. Overlaid for reference are the contours of the X-ray surface brightness at 0.4 – 7 keV by Chandra corresponding to 64, 32, 18, 8, 4, and 2% of the peak value, after being smoothed by a Gaussian kernel with $2.3''$ FWHM. The position of the subtracted AGN is marked by a diamond.

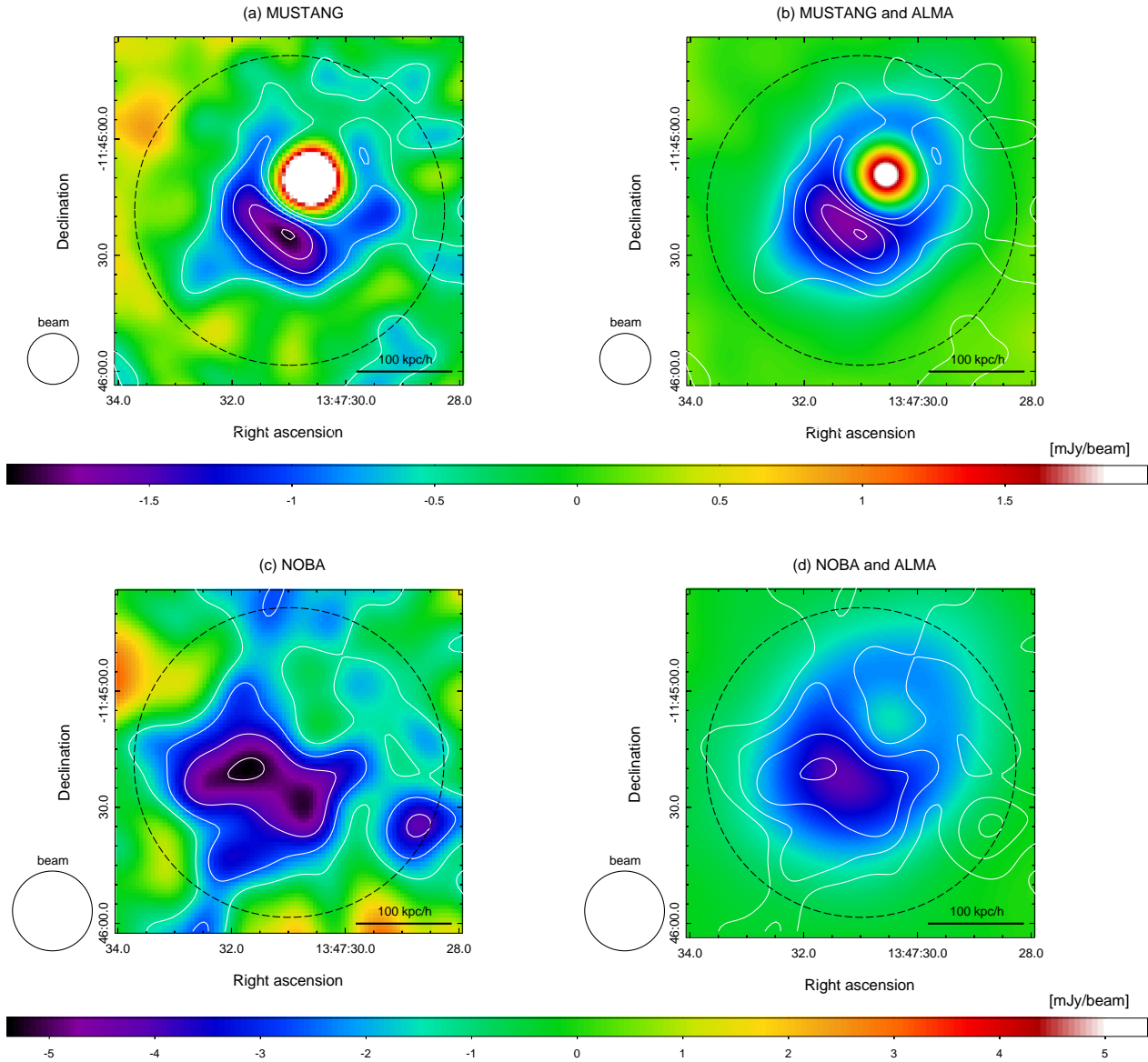


Fig. 13. Comparison of the deconvolved ALMA map with previous SZE observations of RX J1347.5–1145. (a) The MUSTANG map at 90 GHz (Mason et al. 2010; Korngut et al. 2011) processed with an updated pipeline and smoothed to an effective beam size of $13.5''$ FWHM (B. Mason and C. Romero, private communication; Romero et al. 2015). Contours indicate the S/N of 1–5 in 1σ increments with $1\sigma \sim 0.4$ mJy/beam depending on the exposure at each position of the map. (b) The overlay of the contours plotted in panel (a) on the ALMA map corrected for the missing flux, re-added the point source, and smoothed to $13.5''$ FWHM. (c) The NOBA map at 150 GHz (Komatsu et al. 2001) smoothed to an effective beam size of $20.6''$ FWHM. Contours indicate the S/N of 1–4 in 1σ increments with $1\sigma = 1.3$ mJy/beam. (d) The overlay of the contours plotted in panel (c) on the ALMA map converted to 150 GHz, corrected for the missing flux, re-added the point source, and smoothed to $20.6''$ FWHM. Dashed circles indicate the radius of $40''$ from the intensity peak in the unsmoothed ALMA map, at which the mean brightness values (-0.046 mJy/beam and -0.76 mJy/beam) in panels (b) and (d), are set equal to those of panels (a) and (c), respectively.

data, the similar procedure to that mentioned above was applied to the deconvolved ALMA map except that the ALMA map at 92 GHz was converted to 150 GHz by multiplying a factor of 1.14 to correct for the SZE spectrum (this factor includes the relativistic correction and is accurate to better than 0.5% at $kT_e < 25$ keV), the central AGN was added with the flux expected at 150 GHz assuming a power-law spectrum with the index -0.527 (Sayers et al. 2016), and the mean brightness at $40''$ from the peak is taken to be -0.76 mJy/beam.

Morphology of the ALMA map is in good agreement with both MUSTANG and NOBA maps particularly in the south-east region, where the S/N of each measurement is high. It is also evident that eliminating the point source contamination is crucial for

recovering detailed structures of the SZE. The position of the south-east peak in the source-added and smoothed maps (panels b and d) is offset by $\sim 7''$ compared to that identified in the unsmoothed ALMA map (Figure 4). The eastern ridge (the feature labeled as 2 in Figure 5 of Mason et al. 2010) is weaker than reported by Mason et al. (2010) in both ALMA and updated MUSTANG maps. In accord with Mason et al. (2010), a low significance decrement peak in the south-west quadrant of this cluster seen in the NOBA map (the feature labeled as 3 in Figure 5 of Mason et al. 2010) is absent in the ALMA map as well.

With respect to the positions marked by the dashed circles in Figure 13, the peak intensities of the decrement in the source-added and smoothed ALMA maps shown in Figures 13(b)(d) are $-1.70 \pm 0.07 \pm 0.29$ mJy/beam and $-3.39 \pm 0.13 \pm 0.66$ mJy/beam, respectively (the latter is a converted value at 150 GHz); quoted systematic errors are from the missing flux correction and the flux calibration. These intensities are consistent with the corresponding values measured on the MUSTANG map of -1.9 mJy/beam (with the 1σ statistical error of ~ 0.4 mJy/beam) and on the NOBA map of -4.6 ± 1.3 mJy/beam, respectively, within the range of uncertainties in each measurement.

5 Conclusions

In this paper, we have presented the first image of the thermal SZE obtained by ALMA. The resulting angular resolution of $5''$ corresponds to $20h^{-1}$ kpc for our target galaxy cluster RX J1347.5–1145 at $z = 0.451$. The present dataset achieves the highest angular and physical spatial resolutions to date for imaging the SZE. The ALMA image has clearly resolved the bright central AGN, the cool core, and the offsetted SZE peak in this cluster. It is in good agreement with an electron pressure map reconstructed independently from the X-ray data as well as with the previous SZE observations of this cluster by NOBA (Komatsu et al. 2001; Kitayama et al. 2004) and MUSTANG (Mason et al. 2010; Korngut et al. 2011).

The statistical significance of the measurement has also improved significantly; the achieved 1σ sensitivity of the image is 0.017 mJy/beam or 0.12 mK_{CMB} at $5''$ FWHM. The accuracy of the map is limited primarily by missing flux arising from the lack of short-spacing data in the current configuration of ALMA. We have presented detailed analysis procedures including corrections for the missing flux based on realistic imaging simulations for RX J1347.5–1145. We have shown that the structures up to the spatial scale of $40''$ are faithfully recovered in the ALMA map.

Our results demonstrate that ALMA is a powerful instrument for imaging the SZE in compact galaxy clusters with unprecedented angular resolution and sensitivity. They will also serve as guiding methods for analyzing and interpreting future SZE images by ALMA. Completion of the Total Power Array for continuum observations as well as Band 1 receivers will significantly strengthen the capability of ALMA for imaging the SZE. Further implications of the present results on the physics of galaxy clusters will be explored separately in our forthcoming papers.

Acknowledgments

We thank Brian Mason and Charles Romero for providing the MUSTANG map and helpful comments on the manuscript; Akiko Kawamura, Hiroshi Nagai, and Kazuya Saigo for their support on the ALMA data reduction. This paper makes use of the following ALMA data: ADS/JAO.ALMA#2013.1.00246.S. The scientific results of this paper are based in part on data obtained from the Chandra Data Archive: ObsID 506, 507, 3592, 13516, 13999, and 14407. ALMA is a partnership of ESO (representing its member states), NSF (USA) and NINS (Japan), together with NRC (Canada) and NSC and ASIAA (Taiwan), in cooperation with the Republic of Chile. The Joint ALMA Observatory is operated by ESO, AUI/NRAO and NAOJ. The National Radio Astronomy Observatory is a facility of the National Science Foundation operated under cooperative agreement by Associated Universities, Inc. This work was supported by the Grants-in-Aid for Scientific Research by the Japan Society for the Promotion of Science with grant numbers 24340035 (Y.S.), 25400236 (T.K.), 26400218 (M.T.), 15H02073 (R.K.), 15H03639 (T.A.), 15K17610 (S.U.), and 15K17614 (T.A.). T.K. was supported by the ALMA Japan Research Grant of NAOJ Chile Observatory, NAOJ-ALMA-0150.

References

- Adam, R., et al. 2014, *A&A*, 569, A66
 Akaori, T., & Yoshikawa, K. 2012, *PASJ*, 64, 12
 Allen, S. W., Schmidt, R. W., & Fabian, A. C. 2002, *MNRAS*, 335, 256
 AMI Collaboration 2006, *MNRAS*, 369, L1
 Anders, E., & Grevesse, N. 1989, *Geochimica et Cosmochimica Acta*, 53, 197
 Arnaud, K. A. 1996, *Astronomical Data Analysis Software and Systems V*, A.S.P. Conference Series, Vol. 101, p.17
 Benson, B. A., Church, S. E., Ade, P. A. R., Bock, J. J., Ganga, K. M., Henson, C. N., & Thompson, K. L. 2004, *ApJ*, 617, 829
 Birkinshaw, M. 1999, *Phys. Rep.* 310, 97
 Bradač, M., et al. 2008, *ApJ*, 681, 187
 Butler, B. 2012, *ALMA Memo* 594
 Carlstrom, J. E., Holder, G. P., & Reese, E. D. 2002, *ARA&A*, 40, 643
 Carlstrom, J. E., Joy, M., & Grego, L. 1996, 456, L75
 Cavaliere, A. & Fusco-Femiano, R. 1978, *A&A*, 70, 677
 Cornwell, T. J. 2008, *IEEE Journal of Selected Topics in Signal Processing*, Vol. 2, Issue 5, p.793-801
 Ferrari, C., et al. 2011, *A&A*, 534, L12

- Fruscione, A., et al. 2006, *Proceedings of the SPIE*, 6270, id. 62701V
- Gitti, M., & Schindler, S. 2004, *A&A*, 427, L9
- Gitti, M., Ferrari, C., Domainko, W., Feretti, L., & Schindler, S. 2007, *A&A*, 470, L25
- Hasselfield, M., et al. 2013, *J. Cosm. Astropart. Phys.*, 07, 008
- Hincks, A. D. et al. 2010, *ApJS*, 191, 423
- Johnson, R. E., Zuhone, J., Jones, C., Forman, W. R., & Markevitch, M. 2012, *ApJ*, 751, 95
- Jones, M., et al. 1993, *Nature*, 365, 320
- Kalberla, P. M. W., Burton, W. B., Hartmann, Dap, Arnal, E. M., Bajaja, E., Morras, R., & Pöppel, W. G. L. 2006, *A&A*, 440, 775
- Kitayama, T., Komatsu, E., Ota, N., Kuwabara, T., Suto, Y., Yoshikawa, K., Hattori, M., & Matsuo, H. 2004, *PASJ*, 56, 17
- Kitayama, T. 2014, *PTEP*, 6, 06B11124
- Komatsu, E., Kitayama, T., Suto, Y., Hattori, M., Kawabe, R., Matsuo, H., Schindler, S., & Yoshikawa, K. 1999, *ApJ*, 516, L1
- Komatsu, E., et al. 2001, *PASJ*, 53, 57
- Köhlinger, & F., Schmidt, R. W. 2014, *MNRAS*, 437, 1858
- Korngut, P. M., et al. 2011, *ApJ*, 734, 10
- Kreisch, C. D., Machacek, M. E., Jones, C., Randall, S. W. 2016, *arXiv:1607.04674*
- Marriage, T. A., et al. 2011, *ApJ*, 731, 61
- Mason, B. S., et al. 2010, *ApJ*, 716, 739
- McMullin, J. P., Waters, B., Schiebel, D., Young, W., & Golap, K. 2007, *Astronomical Data Analysis Software and Systems XVI (ASP Conf. Ser. 376)*, ed. R. A. Shaw, F. Hill, & D. J. Bell (San Francisco, CA: ASP), 127
- Miranda, M., Sereno, M., de Filippis, E., & Paolillo, M. 2008, *MNRAS*, 385, 511
- Muchovej, S., et al. 2007, *ApJ*, 663, 708
- Narayan, R., & Nityananda, R. 1986, *ARA&A* 24, 127
- Nozawa, S., Itoh, N., & Kohyama, Y. 2005, *A&A*, 440, 39
- Ota, N., et al. 2008, *A&A*, 491, 363
- Plagge, T., et al. 2013, *ApJ*, 770, 112
- Planck Collaboration 2011, *A&A*, 536, A8
- Planck Collaboration 2014, *A&A*, 571, A29
- Planck Collaboration 2015, *arXiv:1502.01589*
- Pointecouteau, E., Giard, M., Benoit, A., Désert, F. X., Aghanim, N., Coron, N., Lamarre, J. M., & Delabrouille, J. 1999, *ApJ*, 519, L115
- Pointecouteau, E., Giard, M., Benoit, A., Désert, F. X., Bernard J.P., Coron, N., & Lamarre, J. M. 2001, *ApJ*, 552, 42
- Reese, E. D., Carlstrom, J. E., Joy, M., Mohr, J. J., Grego, L., & Holzapfel, W. L. 2002, *ApJ*, 581, 53
- Reese, E. D., Kawahara, H., Kitayama, T., Ota, N., Sasaki, S., & Suto, Y. 2010, *ApJ*, 721, 653
- Reichardt, C. L., et al. 2013, *ApJ*, 763, 127
- Rephaeli, Y. 1995, *ARA&A*, 33, 541
- Rich, J. W., de Blok, W. J. G., Cornwell, T. J., Brinks, E., Walter, F., Bagetakos, I., & Kennicutt, R. C., Jr. 2008, *ApJ*, 136, 2897
- Riess, A., et al. 2016, *arXiv:1604.01424*
- Romero, C. E., et al. 2015, *ApJ*, 807, 121
- Sanders, J. S. 2006, *MNRAS*, 371, 829
- Sault, R. J. 1990, *ApJ*, 354, L61
- Sayers, J., et al. 2016, *ApJ*, 820, 101
- Schindler, S., Hattori, M., Neumann, D. M., & Böhringer, H. 1997, *A&A* 317, 646
- Staniszewski, et al. 2009, *ApJ*, 701, 32
- Sunyaev, R. A., & Zel'dovich, Ya. B. 1972, *Comments Astrophys. Space Phys.*, 4, 173
- Takizawa, M. 2005, *ApJ*, 629, 791
- Vanderlinde, K., et al. 2010, *ApJ*, 722, 1180
- Williamson, R., et al. 2011, *ApJ*, 738, 139
- Wu, J-H. P., et al. 2009, *ApJ*, 694, 1619
- Yamada, K., et al. 2012, *PASJ*, 64, 102
- Young, A. H., et al. 2015, *ApJ*, 809, 185
- Zemcov, M., Borys, C., Halpern, M., Mausekopf, P., & Scott, D. 2007, *MNRAS*, 376, 1073
- Zemcov, M., et al. 2012, *ApJ*, 749, 114